Available online at www.sciencedirect.com

ScienceDirect

Journal of Magnesium and Alloys 10 (2022) 266–280

www.elsevier.com/locate/jma

Full Length Article

Effect of multiaxial deformation on structure, mechanical properties, and corrosion resistance of a Mg-Ca alloy

N.Yu. Yurchenko[a], N.D. Stepanov[a], G.A. Salishchev[a], V.N. Serebryany[b], N.S. Martynenko[b,*], E.A. Lukyanova[b], L.L. Rokhlin[b], N. Birbilis[d], S.V. Dobatkin[b,c], Y.Z. Estrin[d,e]

[a] *Belgorod State National Research University, Belgorod, Russia*

[b] *Federal State Budget Institution of Science, A.A. Baikov Institute of Metallurgy and Materials Science, Russian Academy of Sciences, Moscow, Russia*

[c] *National University of Science and Technology "MISiS", Moscow, Russia*

[d] *Department of Materials Engineering, Monash University, Clayton, VIC 3800, Australia*

[e] *Department of Mechanical Engineering, The University of Western Australia, Nedlands WA 6009, Australia*

Received 22 March 2021; received in revised form 5 June 2021; accepted 5 July 2021

Available online 3 August 2021

Abstract

This article provides a report on the effect of multiaxial deformation (MAD) on the structure, texture, mechanical characteristics, and corrosion resistance of the Mg-0.8 (wt.)% Ca alloy. MAD was carried out on the alloy in the as-cast and the annealed states in multiple passes, with a stepwise decrease in the deformation temperature from 450 to 250 °C in 50 °C steps. The cumulative true strain at the end of the process was 22.5. In the case of the as-cast alloy, this resulted in a refined microstructure characterized by an average grain size of 2.7 μm and a fraction of high-angle boundaries (HABs) of 57.6%. The corresponding values for the annealed alloy were 2.1 μm and 68.2%. The predominant mechanism of structure formation was associated with discontinuous and continuous dynamic recrystallization acting in concert. MAD was also shown to lead to the formation of a rather sharp prismatic texture in the as-cast alloy, whilst in the case of the annealed one the texture was weakened. A displacement of the basal poles {00.4} from the periphery to the center of a pole figure was observed. These changes in the microstructure and texture gave rise to a significant improvement of the mechanical characteristics of the alloy. This included an increase of the ultimate tensile strength reaching 308 MPa for annealed material and 264 MPa for the as-cast one in conjunction with a twofold increase in ductility. A further important result of the MAD processing was a reduction of the rate of electrochemical corrosion, as indicated by a significant decrease in the corrosion current density in both microstructural states of the alloy studied.

Keywords: Metals and alloys; Multiaxial deformation; Microstructure; Recrystallization; Mechanical properties; Corrosion.

1. Introduction

Magnesium alloys are widely used as structural materials in aerospace, automotive, and consumer electronics, due to their low density and high specific strength [1,2]. Magnesium and its alloys have also been suggested as promising materials for biomedical applications [3,4]. This is based on a range of their favorable properties that include (i) a combination of low density and relatively high strength, similar to that of cortical bone tissue, (ii) good biocompatibility, (iii) bioresorbability, i.e., the ability to dissolve in physiological environments [5]. The latter property would eliminate the need for surgical extraction of an implant. In this context, magnesium alloys are being widely explored for orthopedic implants, coronary stents, fasteners, etc. [3-9].

A drawback of many magnesium alloys and pure magnesium is an excessively high biodegradation rate. Additionally, their strength is also often insufficient for some applications.

* Corresponding author at: Leninsky prospect, 49, Moscow, Russian Federation, 119334.

E-mail address: nataliasmartynenko@gmail.com (N.S. Martynenko).

https://doi.org/10.1016/j.jma.2021.07.004

Both the corrosion rate and strength of magnesium can be modified by suitable alloying and/or grain refinement. Calcium (Ca), manganese (Mn), zinc (Zn), and zirconium (Zr), are considered important alloying elements for biomedical magnesium alloys since they are non-toxic for the human body and can reduce the biodegradation rate [9-10]. Recently, magnesium alloys with rare-earth elements (Y, Nd, Gd) have been examined with a view of using them for biomedical purposes [11,12].

The properties of the alloys can also be tailored by controlling their microstructure, for example, by refining the grain size. The effective method of grain refinement down to the ultra-fine grain (UFG) scale is severe plastic deformation (SPD) [13]. The most developed SPD methods include high-pressure torsion (HPT) [14-16] and equal-channel angular pressing (ECAP) [17-20]; the capacity of these methods to refine the structure of various metals and alloys was demonstrated in a number of works. Yet there are limitations to their upscaling aimed at large-scale production in an industrial environment. Other SPD methods, more suitable for industrial applications, are therefore of interest. One of these methods is multiaxial deformation (MAD), also known as multi-directional forging (MDF) [21]. The possibility of grain refinement in magnesium alloys by multiaxial deformation was demonstrated in [22-25].

In the present work, a binary low-alloyed Mg-0.8% (wt.%) Ca alloy processed by MAD was examined. Alloying with calcium is considered as a promising approach to developing Mg-based alloys for medical implants because it is an essential element for a number of vital body systems and, in particular, for bone tissue. There is also evidence that Ca can exhibit anticarcinogenic properties [26]. The main effect of SPD on materials and its defining feature is a significant increase in strength – usually at the expense of ductility. However, recently it was shown that SPD can simultaneously increase both strength and the in-service performance of metallic materials, such as wear resistance [27-29], corrosion resistance [30,31], cold resistance [32], fatigue strength [33-35], and electrical conductivity [36,37]. A particular advantage of MAD as applied to Mg alloys is its ability to produce crystallographic texture favorable to their property profile.

These considerations have guided us in our selection of the alloy (Mg-0.8% Ca) and the process (MAD) for this study. The effect of processing by MAD on the microstructure, texture, mechanical properties, and corrosion resistance of the alloy is reported below.

2. Experimental

Magnesium alloy Mg-0.8% (wt.%) Ca (henceforth designated as Mg-0.8% Ca alloy for simplicity) was melted in an electric resistance furnace in a metal crucible and cast in a thick-walled steel mold heated to 150 - 200 °C to an ingot of 40 mm diameter and 120 mm length. Specimens from the alloy ingot were heat treated in a muffle furnace for 6 hours at a temperature of 510 °C, and then quenched in water. After heat treatment, two types of cylindrical billets for MAD processing were cut. Small billets (Ø10 mm × 14 mm length) were used for microstructure investigations, while large billets (Ø15 mm × 35 mm length) were used for mechanical testing.

The compression tests at a constant rate of 1 mm/min were conducted using an Instron 300LX hydraulic machine equipped with a radial heating furnace at temperatures of 250°C, 300°C, 350°C, 400°C, and 450°C. The samples were deformed to 75% strain or to failure if it occurred at a lower strain. MAD was carried out using the same machine at constant deformation rates of 1 or 2 mm/min for samples of 10 mm diameter and 14 mm length or 15 mm diameter and 35 mm length, respectively. The first pass of MAD was performed at a temperature of 450°C; a next pass and the following ones were conducted at a temperature lowered by 50 °C. Nine passes in total were performed - the last one at a temperature of 250 °C. Further decrease of MAD temperature resulted in pronounced cracking of the specimens and was therefore not pursued. Stress-strain curves were recorded during each individual compression step and were used to determine the flow stress as a function of the deformation temperature. The true strain per pass was roughly estimated as 2.5; the cumulative true strain amounted to 22.5. Smaller samples of the alloy (Ø10 mm × 14 mm) in annealed condition were used to investigate the microstructure evolution during MAD, while larger samples (Ø15 mm × 35 mm) of the alloy both in the as-cast and the annealed conditions were used to study the microstructure and the mechanical and corrosion properties after nine MAD passes.

Specimens for metallographic examination were prepared by grinding the samples with gradual reduction of the paper grit and final polishing using an O-PS (SiC) suspension. Afterwards, the specimens were etched using a mixture of 100 ml of ethanol, 5 g of picric acid, 5 ml of acetic acid, and 10 ml of distilled water. Metallographic examination of the specimens was performed with an Olympus GX71 optical microscope. The average grain size was measured by the linear intersects method using the ImageScope software (Leica, Germany).

Further microstructure examination was carried out with an FEI Quanta 200 3D and a Nova NanoSEM 450 FEI scanning electron microscopes (SEMs) equipped with back-scattered electrons (BSE), energy dispersive spectrometry (EDS), and electron back-scattered diffraction (EBSD) detectors. The OIM Analysis 6.2 software was used for the EBSD analysis and data processing. In the orientation maps presented, high-angle boundaries ($\theta > 15°$) and low-angle boundaries ($2° < \theta < 15°$) are indicated by black and white lines, respectively.

For phase identification, a RIGAKU Ultima IV X-ray diffractometer (XRD) with the CuKα radiation was used. The texture in the longitudinal direction was examined with a DRON-7 X-ray texture diffractometer with the CoKα radiation in the reflection mode by recording six incomplete pole figures, {10.0}, {10.1}, {10.2}, {11.0}, {10.3}, and {00.4}, at a maximum inclination angle $\alpha_{max} = 70°$ at a step of 5° for the α and β angles (0-360°), where α and β are the radial and azimuth angles on the pole figure, respectively. The

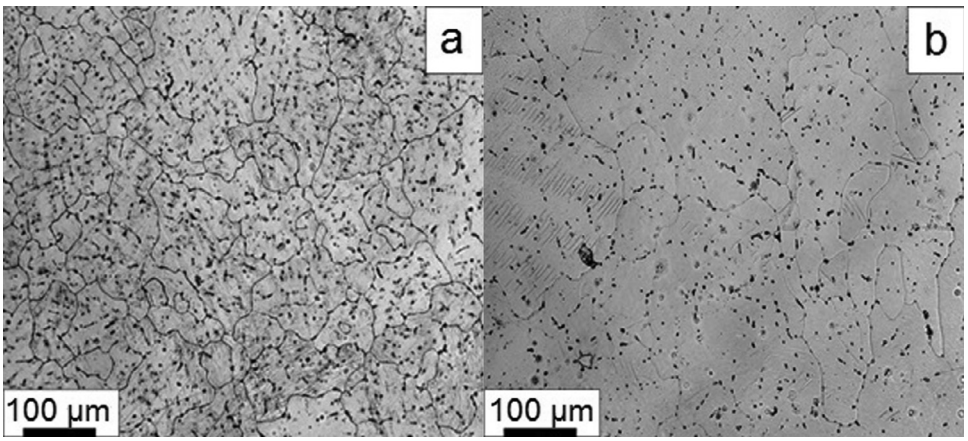

Fig. 1. Microstructure of the Mg-0.8% Ca alloy in (a) the as-cast and (b) the annealed conditions (optical microscopy).

X-ray measurements were performed on a section parallel to the last loading direction of MAD. The orientation distribution functions (ODFs) were reconstructed from the measured pole figures by an approximation based on a large number (1000) of Gaussian normal distributions [38].

The quantitative analysis of textures by the above approximation method allowed evaluating the generalized Schmid factors for effective deformation mechanisms in the material under study. To evaluate the orientation factors, which depend on the generalized Schmid factors, the following relations were used [39]:

$$M_i = \frac{1}{m_i}, \tag{1}$$

where m_i are the generalized Schmid factors for basal, prismatic, and pyramidal slip and twinning. They can be estimated for a chosen deformation system and the texture of the alloy from the relation:

$$m_i = \sum_{j=1}^{p} m_{ij} W_j, \tag{2}$$

where m_{ij} is the Schmid orientation factor calculated for the i-th slip system and j-th texture component, W_j is the volume fraction of the j-th texture component, and p is the number of texture components.

Tensile tests were performed using dog-bone shaped specimens with a gauge length of 16 mm, width of 3 mm, and thickness of 1.5 mm. Mechanical testing was performed on an Instron-5882 machine. The tests were carried out at room temperature with an initial strain rate of 1×10^{-3} s^{-1}. Three tests per each condition were conducted.

The corrosion resistance of the Mg-0.8% Ca alloy was evaluated in a 0.9% NaCl solution (physiological solution, pH = 7) at room temperature by the potentiodynamic polarization method [40]. This method reveals the occurrence of corrosion and provides information about the reaction rate [40] and is often used to study binary Mg-Ca alloys [41,42]. A VMP potentiostat equipped with an EC-Lab software (BioLogic) was used. A PAR flat cell (Princeton Applied Research) with a three-electrode configuration (working electrode, saturated calomel electrode, and platinum counter electrode) was used for testing. Before potentiodynamic scanning, the samples were preliminarily ground with abrasive papers with a gradual reduction in the grit size (from P800 to P2500) and cleaned with ethanol. Scanning was performed in a range from 100 mV below the previously measured open circuit potential (OCP) to -1000 mV at a rate of 1 mV/s. Each sample was scanned five times. Between the scans, the samples were polished and cleaned.

3. Results

3.1. Microstructure of the Mg-0.8% Ca alloy

3.1.1. Structure of the alloy prior to multiaxial deformation

Fig. 1a shows an optical micrograph of the as-cast structure of the Mg-0.8% Ca alloy. The structure comprises a magnesium matrix and particles that appear dark in the OM image (Fig. 1a). The average size of the matrix grains is 61 μm with a scatter from 18 to 165 μm (Fig. 1a). The particles are located at grain boundaries and form a continuous layer with an average thickness of ~1.1 μm. The volume fraction of these particles was estimated at 1.5%. Second-phase particles are also present inside the matrix grains. These are distributed rather uniformly and are either equiaxed or oblong. Their characteristic size and volume fraction are ~ 2.5 μm and 3.2%, respectively (Fig. 1a). According to the XRD data, the second phase was identified as the intermetallic compound Mg_2Ca (Fig. 2a). The calcium content in the matrix in the as-cast condition determined by SEM-EDS analysis was 0.29 ± 0.03 wt.%.

Fig. 1b shows the microstructure of the Mg-0.8% Ca alloy after annealing treatment. The average grain size after annealing is seen to have risen to 95 μm with a scatter between 37 and 233 μm. The second-phase layer at the grain boundaries has disappeared. Instead, rather coarse equiaxed particles (with the average size of ~2.5 μm) located on the grain boundaries are seen. The volume fraction of these particles is 1.5%. The presence of fine, homogeneously distributed equiaxed particles with the average size of ~0.3 μm and the

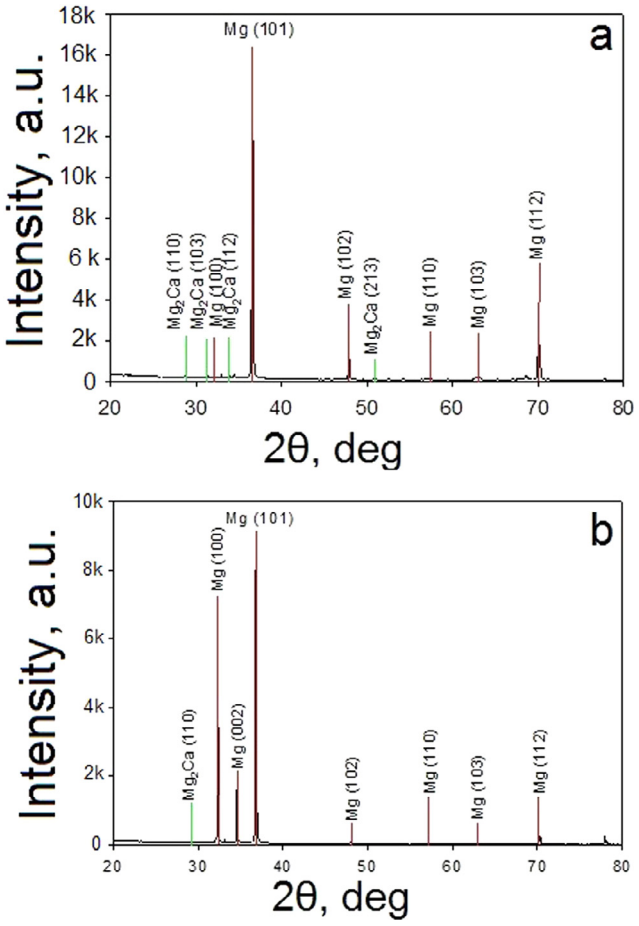

Fig. 2. XRD patterns of the Mg-0.8% Ca alloy in (a) the as-cast and (b) the annealed conditions.

volume fraction of ~1% populating the interior of the matrix grains is observed (Fig. 1b). The results of the XRD analysis (Fig. 2b) also suggest that a certain amount of the intermetallic Mg_2Ca particles have dissolved during annealing – also confirmed by the increased calcium content in the matrix (to 0.57 ± 0.04 (wt.%)), as determined by SEM-EDS.

3.1.2. Mechanical behavior of the Mg-0.8% Ca alloy during uniaxial compression in the as-cast and the annealed conditions

Fig. 3 shows the engineering stress-strain curves of the alloy at different test temperatures in the as-cast and the annealed conditions. The yield strength and the overall deformation curves are lower for higher deformation temperatures. The shape of the curves also changes. A prolonged strain hardening stage is characteristic of the deformation in the temperature interval of 250-300˚C in both structural states of the material, but the character of strain hardening as reflected in the shape of stress-strain curves is significantly different. At higher temperatures (400-450˚C) a nearly steady state plastic flow is observed after yielding. The annealed alloy exhibits a lower yield point, but significantly higher flow stresses in the strain interval from 5-10% to 20-30%. At these high temperatures (400-450˚C) the differences between the deformation curves of the annealed and the as-cast alloys nearly vanish.

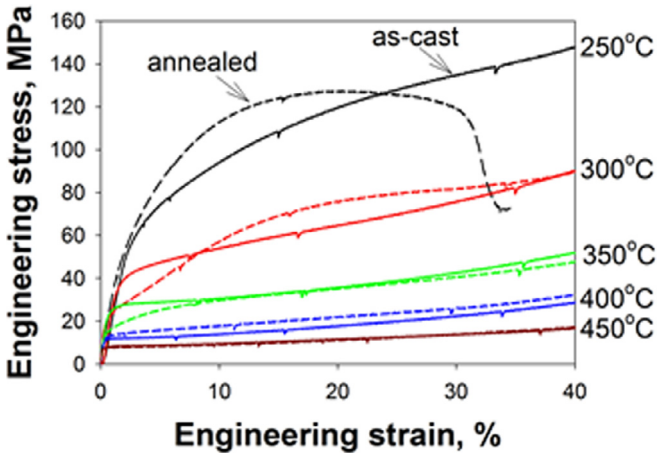

Fig. 3. Temperature dependence of the stress-strain curves for the Mg-0.8% Ca alloy under uniaxial compression in the as-cast (solid lines) and the annealed (dashed lines) conditions.

3.1.3. Microstructure evolution during uniaxial compression

Fig. 4 displays microstructures of Mg-0.8%Ca in the as-cast (a,c,e) and the annealed (b,d,f) states after uniaxial compression at 250, 350, and 450°C up to a strain of 75%. At 250 °C, the microstructure is inhomogeneous for both states (Fig. 4a, b). The initial grains are elongated in the deformation direction and shear bands are visible, especially in the annealed state. Fine recrystallized grains are clearly seen along the boundaries of the initial grains and inside the shear bands. The average grain size in the as-cast and the annealed state is, respectively, ~ 2 μm and ~ 0.8 μm.

An increase in the deformation temperature to 350 °C is seen to give rise to an increase of the fraction of recrystallized grains. Their average size rises to ~ 6 μm in the as-cast and ~ 3 μm in the annealed material (Fig. 4c, d). Further increase in the deformation temperature to 450 °C leads to the formation of a fully recrystallized microstructure with an average grain size of 23 μm and 20.5 μm and a large fraction of high-angle grain boundaries (68.4 and 75.5%) in the as-cast and the annealed conditions, respectively (Fig. 4e, f).

3.1.4. Microstructure evolution during multiaxial deformation

The EBSD IPF maps of the structure of the Mg-0.8% Ca alloy in the annealed state after 1, 3, 5, 7, and 9 passes of MAD with a stepwise decrease of the deformation temperature (the first pass ending at 450 °C, the third at 400 °C, the fifth at 350 °C, the seventh at 300 °C, and the ninth at 250 °C) are presented in Fig. 5. Fig. 6 shows the average recrystallized grain size as a function of the deformation temperature. Note that optical microscopy returned grain size values very similar to those obtained by EBSD. Fig. 5a demonstrates that a non-homogeneous recrystallized structure in which regions of relatively fine grains coexist with coarse grained regions

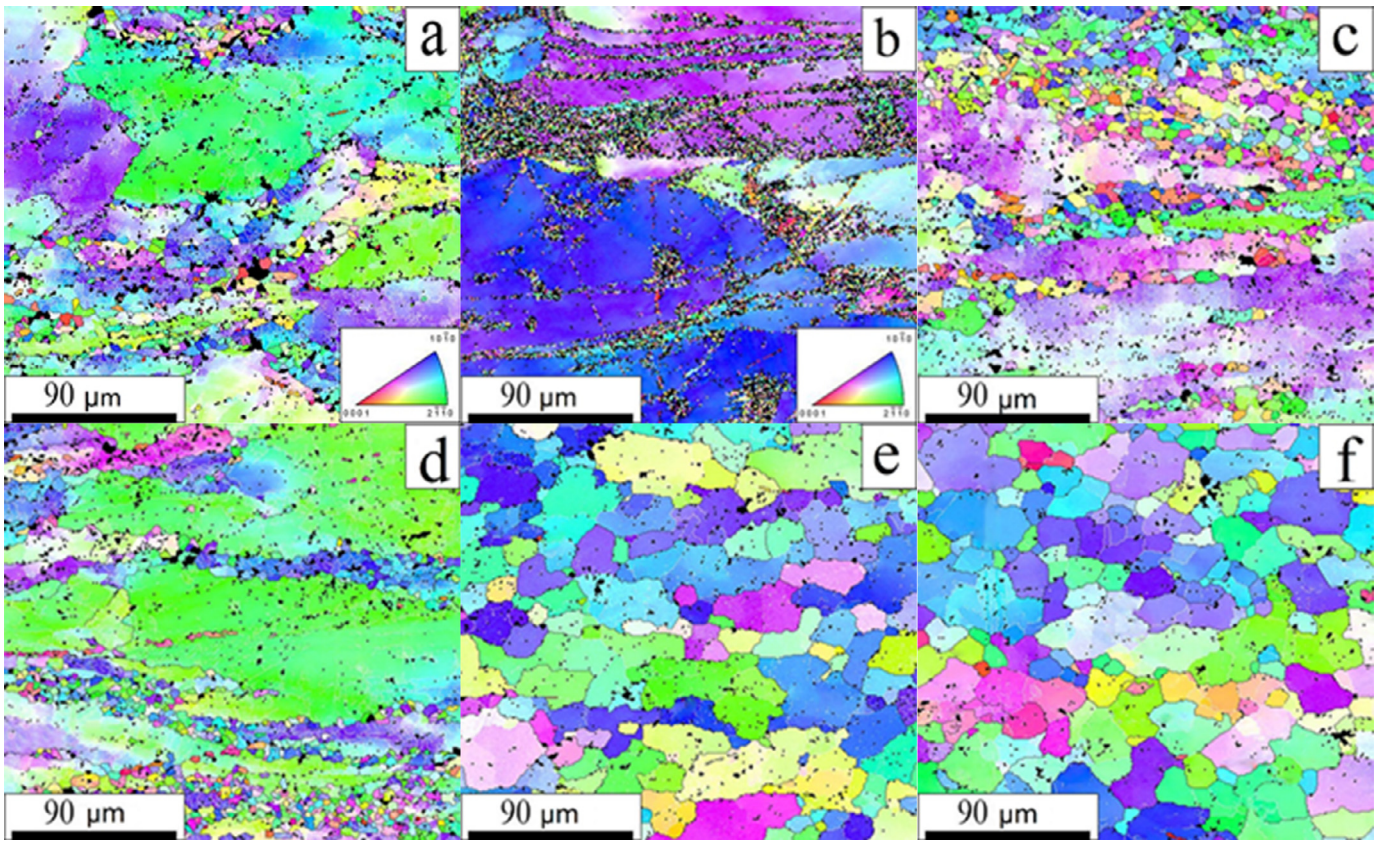

Fig. 4. Microstructure after a compression test to 75% strain at 250°C (a, b), 350°C (c, d), and 450°C (e, f) of the Mg-0.8% Ca alloy in the as-cast (a, c, e) and the annealed state (b, d, f).

have formed already after the first pass of MAD. The average grain of 17.7 μm determined after the first pass (Fig. 6) dropped to ~15.0 μm after three passes. At this stage, the microstructure remained highly non-uniform (Fig. 5b). With further straining, the trend of decreasing grain size with the number of passes continues. The respective average grain size values were 8.9, 3.4, and 2.1 μm after 5, 7, and 9 passes (Fig. 6). The microstructure became noticeably more homogeneous, especially after 5 (Fig. 5c) and 9 (Fig. 5e) passes. The fraction of high-angle boundaries (HABs) varied around ~40-60% over the first 1-7 passes with an increase to 69.3% after 9 passes.

Fig. 7 illustrates the evolution of the second-phase particles in the Mg-0.8% Ca alloy during MAD with SEM-BSE images. The micrographs show a clear picture of a bimodal distribution of the particles with coarse, irregularly shaped particles coexisting with fine round ones. The coarse particles seem to be largely unaffected by deformation, while both the size and the fraction of the fine particles did evolve with strain. The size of the coarse particles (~3.5-4.5 μm) practically did not depend on the deformation temperature. Fracturing of some particles after 9 passes (deformation at 250 °C) (cf. e.g. Fig. 7e, upper left corner) is to be mentioned. Fig. 8 shows the dependence of the average size of fine round particles and the fraction of both fine and coarse second-phase particles on the temperature of MAD. The average size of the fine particles was ~0.6 μm after the first forging pass; from the third pass on it started to increase monotonically and reached a level of ~1 μm after 9 passes. Concurrently, the total volume fraction of the particles increased from 5.8% after 3 passes to 7.3% after 9 passes.

The difference in the structure of the as-cast and the annealed state can affect the formation of the microstructure during the MAD of large samples required for studying various characteristics of the alloy. Therefore, in analyzing the above data on the evolution of the structure of the annealed alloy during the processing of large samples, the as-cast state was also considered. Fig. 9 shows the EBSD orientation maps of large samples taken in as-cast (Fig. 9a) and the annealed (Fig. 9b) conditions and then deformed by 9 MAD passes. The structure of the alloy that was annealed and then MAD-processed comprised grains with an average size of 2.1 μm. The fraction of HABs was 68.2%. Note that the microstructures of the small and large samples of the annealed alloy were very similar (cf. Figs. 7e and 9b). A comparison of Fig. 9a and b shows that the structure of the annealed and subsequently deformed alloy is more homogeneous than that of the as-cast alloy. The occurrence of some coarse grains with curved boundaries surrounded by necklaces of finer equiaxed grains suggests incomplete recrystallization (Fig. 9a) as well as a lower fraction of HABs, namely 57.6%. The average grain size after MAD of the as-cast material was 2.7 μm.

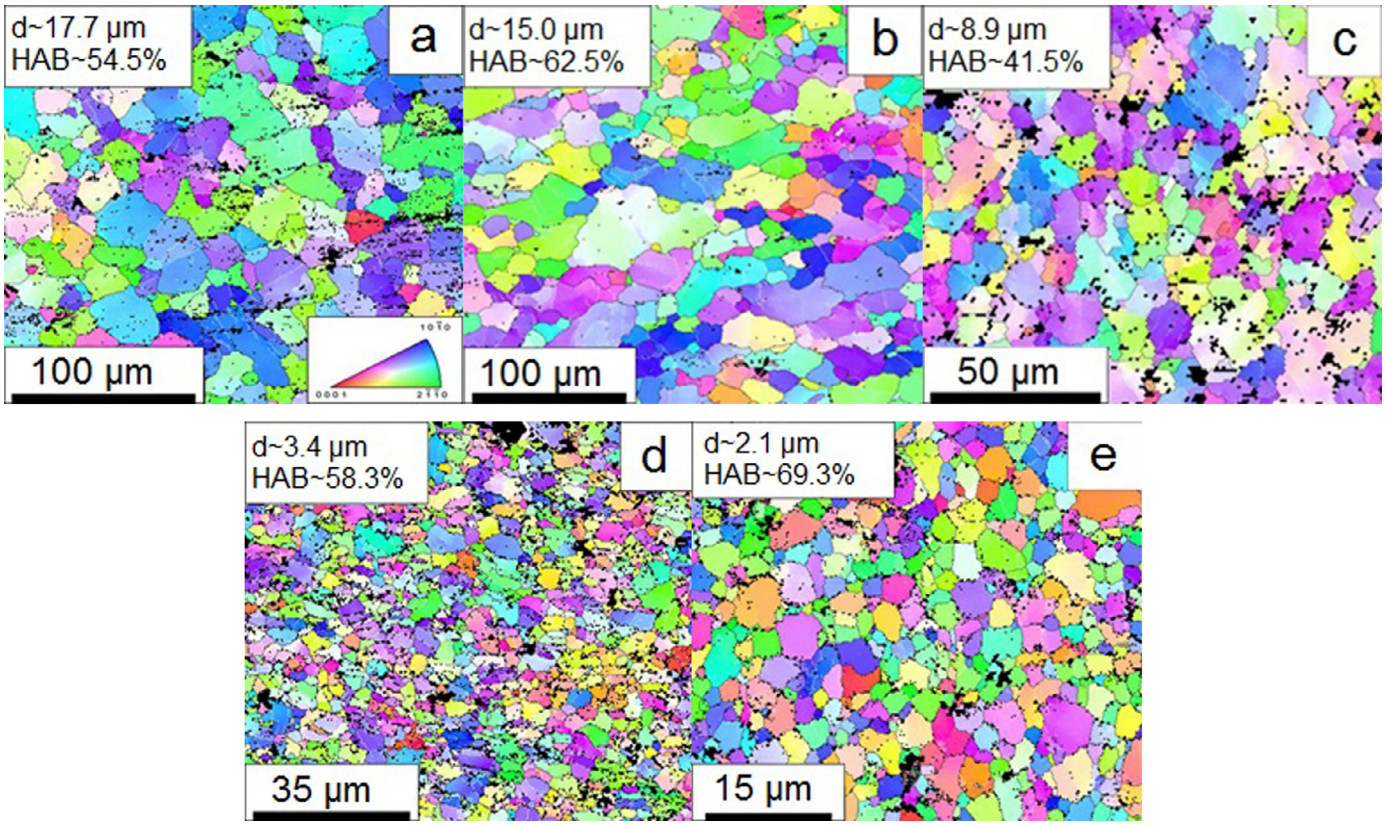

Fig. 5. EBSD orientation maps of the annealed Mg-0.8% Ca alloy after (a) 1, (b) 3, (c) 5, (d) 7, and (e) 9 passes of multiaxial deformation. The color-coding key is given in Fig. 5a.

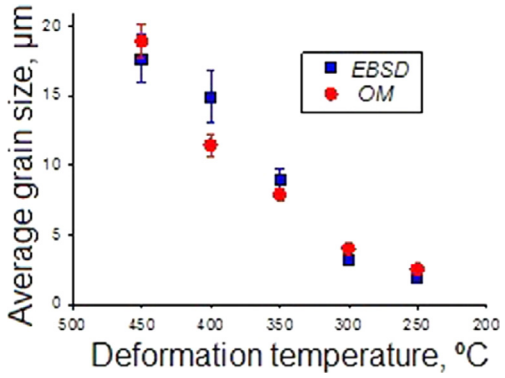

Fig. 6. Average grain size measured by optical microscopy (OM) and EBSD as a function of the multiaxial deformation temperature.

Fig. 10 shows SEM-BSE images of the second-phase particles in the Mg-0.8% Ca alloy in different conditions. In the as-cast and deformed conditions (Fig. 10a) the Mg_2Ca particles were often oblong, while in the case of annealing performed prior to deformation the particles were predominantly equiaxed. In the as-cast and then deformed alloy the average particle size was 1.6 μm, but some larger particles with a size of up to ~5 μm were also found (Fig. 10a). The volume fraction of the particles was 6.1%. The annealed + MAD-processed alloy also contained some large particles (Fig. 10b), yet the average particle size was considerably smaller (~1 μm). The volume fraction of the particles in this condition was 6.5%.

Table 1
Main crystallographic orientations and their volume fractions in the Mg-0.8% Ca alloy after annealing.

No.	(hkil)<uvtw>	φ_1	Φ	φ_2	W
1	$(9.18.\bar{9}2) < 2\bar{1}\bar{1}.14 >$	84	86	0	0.02
2	$(\bar{1}3\bar{2}8) < 2\bar{2}01 >$	58	31	10	0.02
3	$(\bar{2}9\bar{7}.17) < 0\bar{1}11 >$	100	47	20	0.02
4	$(15\bar{6}.12) < \bar{1}\bar{0}.195 >$	139	38	40	0.02
5	$(59.\bar{1}\bar{4}.16) < 1\bar{5}46 >$	70	51	50	0.04
6	$(24\bar{6}3) < 1\bar{5}4.14 >$	82	76	50	0.02
7	Non-textured component				0.86

3.2. Texture of the Mg-0.8% Ca alloy

3.2.1. Texture of the alloy in the as-cast and the annealed conditions

Fig. 11a and b show the {00.4} and {10.0} pole figures and the ODF sections for given Euler (φ_2) angles of the alloy in the as-cast and the annealed conditions, respectively. Table 1 presents the main components of the texture of the annealed alloy. It is evident that in this condition the texture is very weak. The fraction of the non-textured constituent is as high as 0.86. Weak preferential prismatic $(9.18.\bar{9}2) < 2\bar{1}\bar{1}.14 >$, $(24\bar{6}3) < 1\bar{5}4.14 >$ and deflected

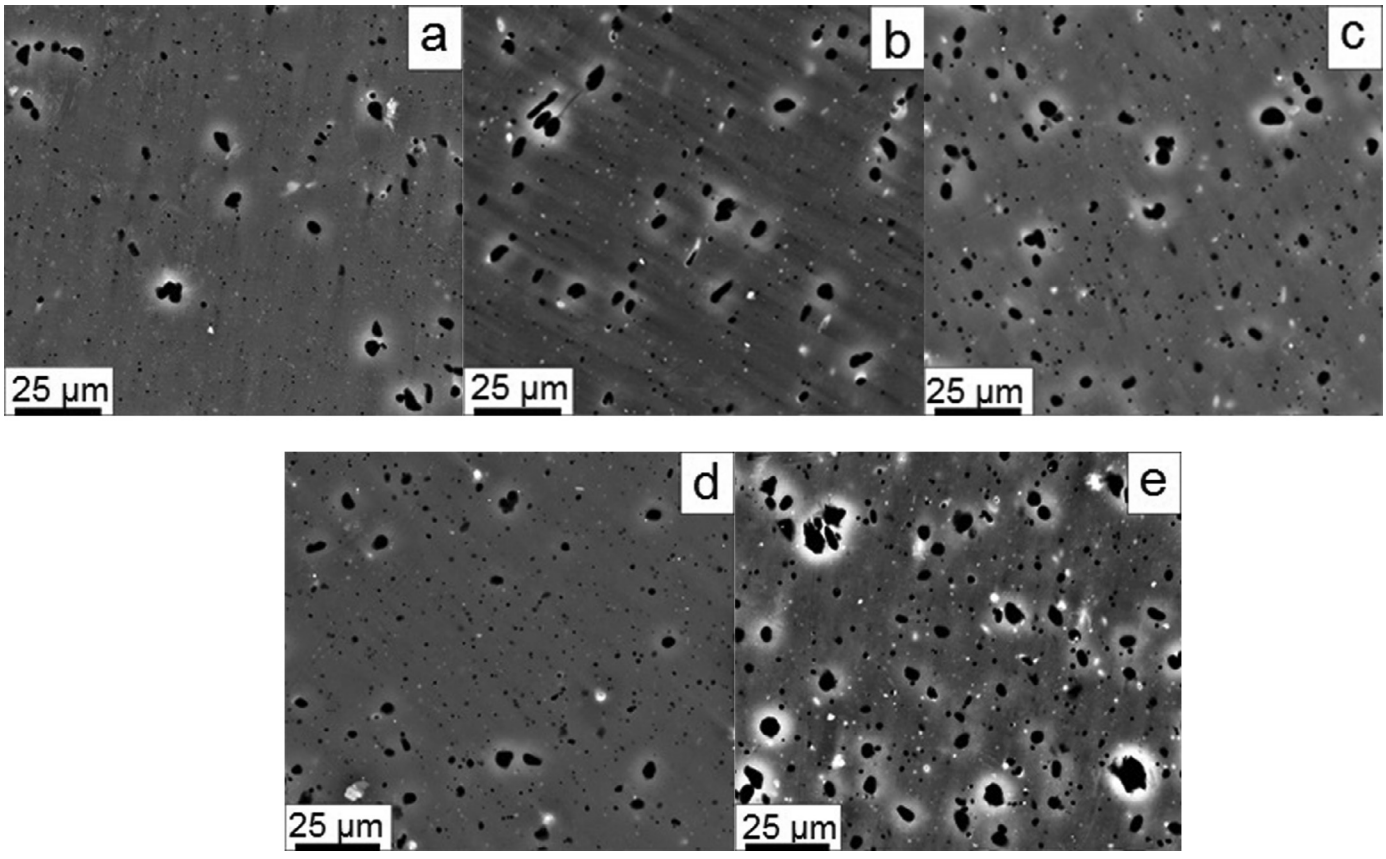

Fig. 7. SEM-BSE images of the annealed Mg-0.8% Ca alloy after (a) 1, (b) 3, (c) 5, (d) 7, and (e) 9 passes of multiaxial deformation.

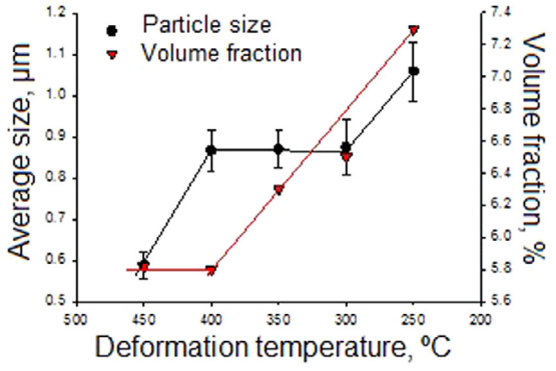

Fig. 8. Average particle size and the volume fraction of the second phase as a function of temperature of the multiaxial deformation of the annealed Mg-0.8% Ca alloy.

basal $(59.\bar{1}4.16) < 1\bar{5}46 >$, $(\bar{1}3\bar{2}8) < 2\bar{2}01 >$, $(\bar{2}9\bar{7}.17) < 0\bar{1}11 >$ orientations with a total fraction of 0.14 were also detected (see Table 1).

3.2.2. Texture after multiaxial deformation

Fig. 11c and d show the data on the texture of the as-cast and the annealed samples after MAD. The quantitative information is presented in Table 2. MAD of the as-cast alloy has resulted in the formation of relatively sharp prismatic texture (Fig. 11c), which is typical for magnesium alloys after similar processing [22]. In this condition, the fractions of the main preferred orientations and the non-textured component were 0.23 and 0.77, respectively (see Table 2). MAD of the annealed alloy has produced a considerably different texture (Fig. 11d). On the {00.4} basal pole figure, the basal poles have moved from the periphery toward the pole figure center. The texture has also become much weaker. The main orientations make up a total fraction of just 0.1, the rest (0.9) being associated with the non-textured component.

Table 2
Main crystallographic orientations and their volume fractions in the Mg-0.8% Ca alloy after MAD.

Alloy state	No.	(hkil)<uvtw>	φ_1	Φ	φ_2	W
As-	1	$(48.\bar{1}\bar{2}.1) < 7\bar{6}\bar{1}8 >$	55	87	50	0.10
cast	2	$(\bar{1}2\bar{1}0) < \bar{1}012 >$	119	90	30	0.04
state + MAD	3	$(06\bar{6}1) < 5\bar{3}\bar{2}6 >$	54	85	30	0.04
	4	$(36\bar{9}1) < \bar{3}216 >$	115	86	50	0.05
	5	Non-textured component				0.77
Annealed	1	$(38.\bar{1}\bar{1}.13) < 12.\bar{1}\bar{7}.5.12 >$	47	55	45	0.02
state + MAD	2	$(\bar{1}2\bar{1}3) < 11.\bar{6}\bar{5}6 >$	45	49	0	0.03
	3	$(\bar{1}2\bar{1}2) < \bar{7}\bar{4}.11.6 >$	144	56	0	0.03
	4	$(\bar{2}5\bar{3}4) < 5\bar{3}\bar{2}5 >$	55	64	5	0.02
	5	Non-textured component				0.90

3.3. Mechanical properties of the Mg-0.8% Ca alloy

Fig. 12 shows the stress-strain curves obtained in uniaxial tensile tests of the Mg-0.8% Ca alloy at room temperature.

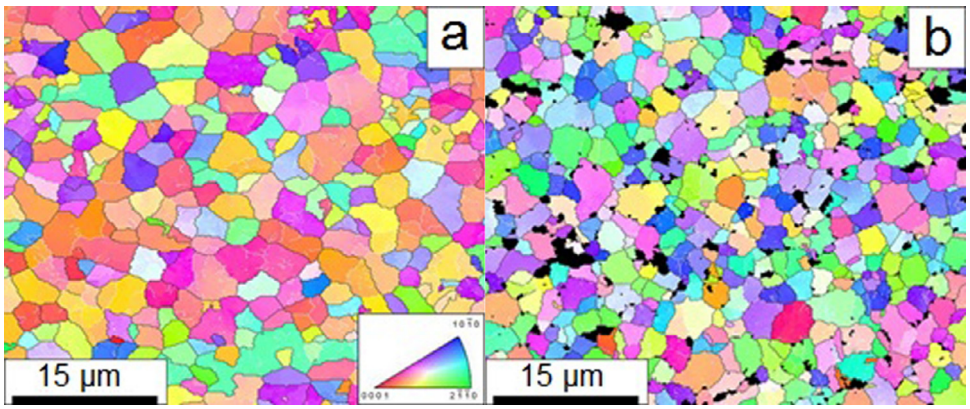

Fig. 9. EBSD orientation maps of the Mg-0.8% Ca alloy after 9 MAD passes: (a) as-cast + MAD-processed; (b) annealing + MAD-processed. The color-coding key is given in Fig. 9 a.

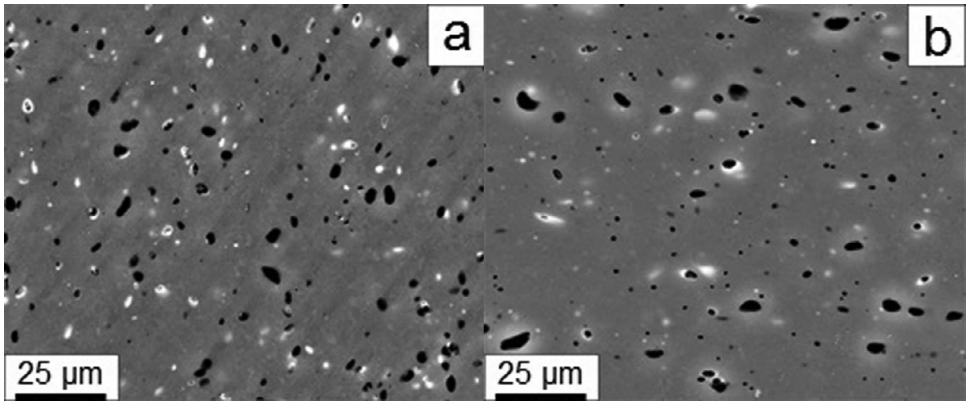

Fig. 10. SEM-BSE images of the Mg-0.8% Ca alloy after 9 passes of multiaxial deformation; condition prior to deformation: (a) as-cast; (b) annealed.

Table 3
Room-temperature mechanical properties of the Mg-0.8% Ca alloy in different conditions .

State	YS, MPa	UTS, MPa	EL, %
As-cast	51	97	4.1
Annealed	50	78	3.0
As-cast + MAD	199	264	9.4
Annealed +MAD	193	308	7.2

The yield strength (YS), the ultimate tensile strength (UTS), and the elongation to fracture (EF) are given in Table 3. In the as-cast state, the alloy exhibits a low strength: the yield strength and the ultimate tensile strength have the values of 51 and 97 MPa, respectively. The ductility of the as-cast alloy is also low, the elongation to fracture being only 4.1%. A result of annealing is some deterioration of mechanical properties; for example, the UTS and the EF dropped to 78 MPa and 3.0%, respectively. A similarity of the shape of the stress-strain curves, with a pronounced hardening stage, for both the as-cast and the annealed alloy should be noted.

MAD processing is seen to have a substantial effect on the mechanical behavior of the alloy (Fig. 12). The stress-strain curve exhibits a short, yet pronounced, hardening stage after yielding, followed by a prolonged stage of nearly steady state flow. It is also seen from Table 3 that both strength and ductility rose owing to MAD treatment. For example, the yield strength increased nearly fourfold and reached 193-199 MPa. The elongation to fracture also increased and reached 7.2-9.4%. Note that unlike the unprocessed alloy, the annealed material had a substantially higher UTS (308 MPa) than the as-cast one (264 MPa).

3.4. Corrosion properties of the Mg-0.8% Ca alloy

The alloy dissolution in 0.9% NaCl solution (physiological solution, pH = 7) is revealed in Fig. 13, which shows the performance of the alloy in the as-cast and the annealed conditions before and after MAD from potentiodynamic polarization (PDP) results. As revealed by electrochemical corrosion rate testing, a significantly improved corrosion resistance and a reduced corrosion rate of the alloy was achieved by MAD. For example, in the as-cast condition, the corrosion potential of the alloy was -1,595 ± 11 mV, and the corrosion current density was 190.61 ± 55.19 μA/cm^2 (Fig. 13a). After MAD, the respective values were -1,507 ± 18 mV and 103.63 ± 23.30 μA/cm^2. Similarly, the corrosion potential and the corrosion current density of the alloy in the annealed condition (-1,581 ± 12 mV and 237.30 ± 13.27 μA/cm^2, respectively) (Fig. 13b) were altered by MAD to -1,536 ± 9 mV and

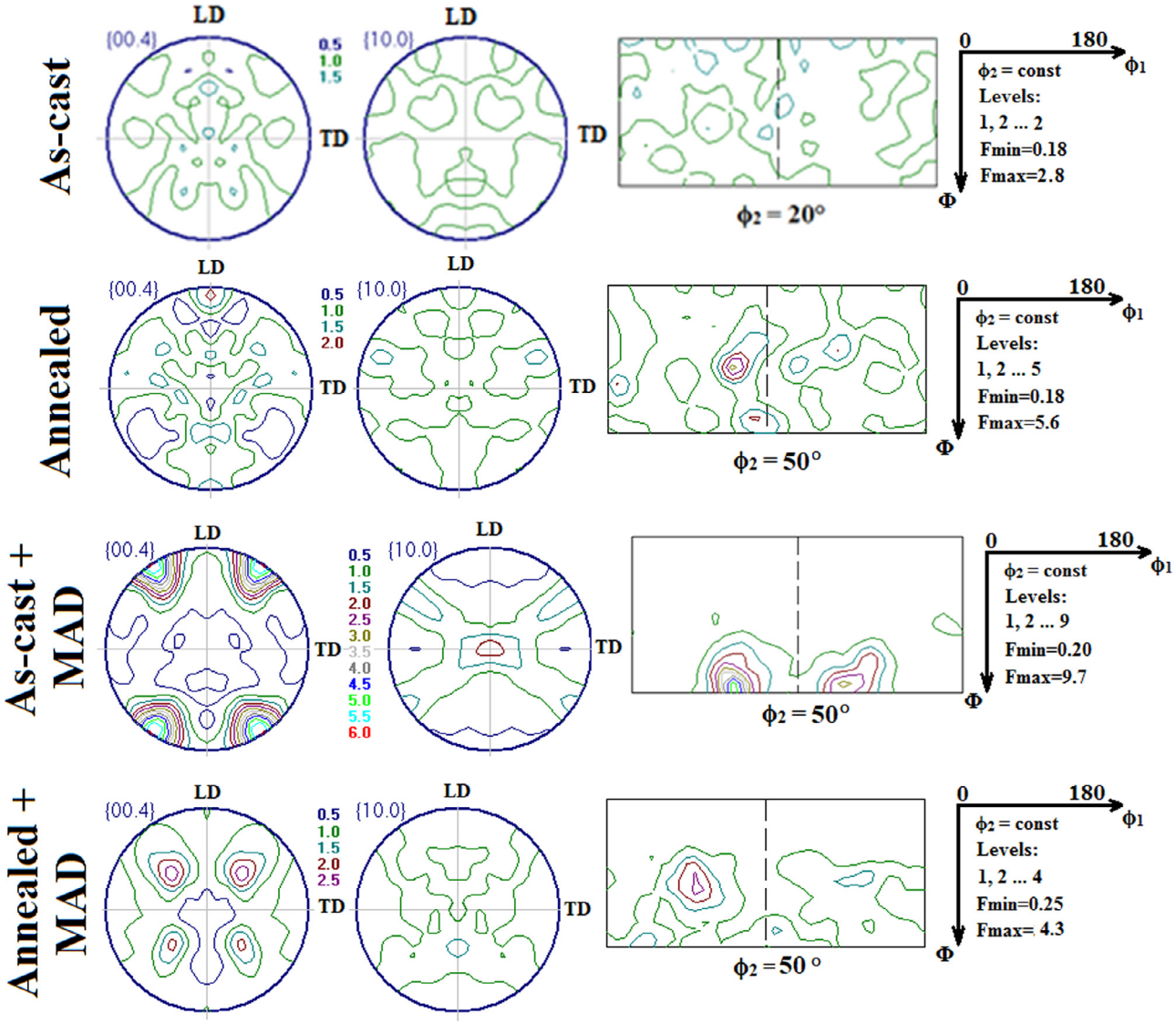

Fig. 11. The (00.4) and (11.0) pole figures and ODF sections for φ_2 = const of the Mg-0.8% Ca alloy in different conditions.

123.36 ± 19.03 μA/cm^2 (Fig. 13). Note that the as-cast alloy had very similar corrosion characteristics before and after annealing. the same remained valid after MAD (Fig. 13c).

4. Discussion

The present study has demonstrated that MAD can be efficiently used to refine the structure and alter the texture of the Mg-0.8% Ca alloy in the as-cast and the annealed states. Through this kind of processing, the mechanical and corrosion properties of the alloy can be improved. To establish the best possible MAD processing conditions, hot compression tests at various temperatures were performed (Figs. 3 and 4). It was found that compression at 250˚C - the lower end of the temperature range considered - resulted in the formation of very fine (∼1 μm sized) grains. However, the fraction of recrystallized grains was low. To achieve a reasonably homogeneous structure, a deformation temperature of 450˚C is required. Therefore, MAD processing was started at 450˚C, followed by a stepwise decrease of the deformation temperature at each subsequent MAD pass, ending at 250˚C. Such processing schedule enabled the production of the material with a homogeneous structure and the average grain size of ∼2-3 μm.

Fig. 14 shows the dependence of the flow stress during MAD on the average grain size determined by optical microscopy and EBSD analysis. A linear relation with a line slope of -1 was found. We hypothesize that this relation is governed by two processes, *discontinuous dynamic recrystallization* (DDRX) and *continuous dynamic recrystallization* (CDRX), acting in concert. Indeed, DDRX is known to operate in magnesium alloys at high temperatures, such as 450 °C [43], whilst CDRX would set in at later deformation steps, as the temperature is dropped to 250 °C [44] DDRX is repetitive in nature. A recrystallized grain would undergo the stages of hot work hardening and dynamic recovery anew, until a critical strain is reached again, after which a repeat recrystallization would occur. Thus, the population of recrystallized

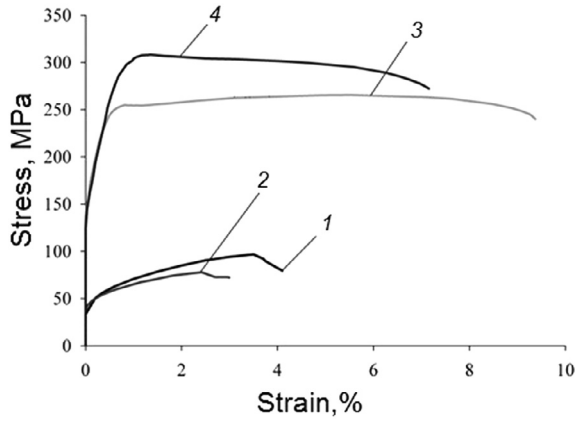

Fig. 12. Stress-strain curves for uniaxial tensile tests conducted at room temperature on the Mg-0.8% Ca alloy in different conditions: 1 - as-cast; 2 - annealed; 3 - as-cast + MAD; 4 – annealed + MAD.

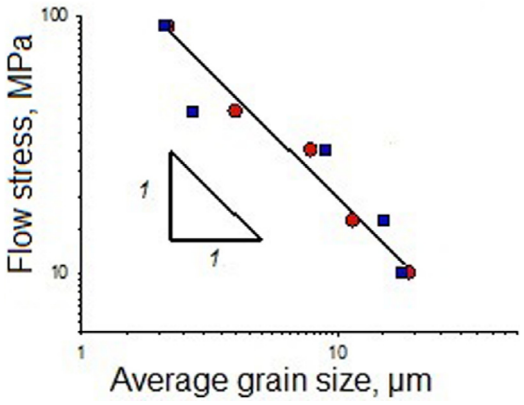

Fig. 14. Relationship between the flow stress after various MAD passes and the corresponding average grain size. The grain size was measured by optical microscopy (OM) and EBSD; both sets of data are presented.

grains will be comprised by grains that are at different stages of microstructure evolution, and this will affect the fraction of high-angle boundaries, as determined by the EBSD method. For example, after the 5th pass of MAD a significant fraction of the subgrain structure with low-angle boundaries was

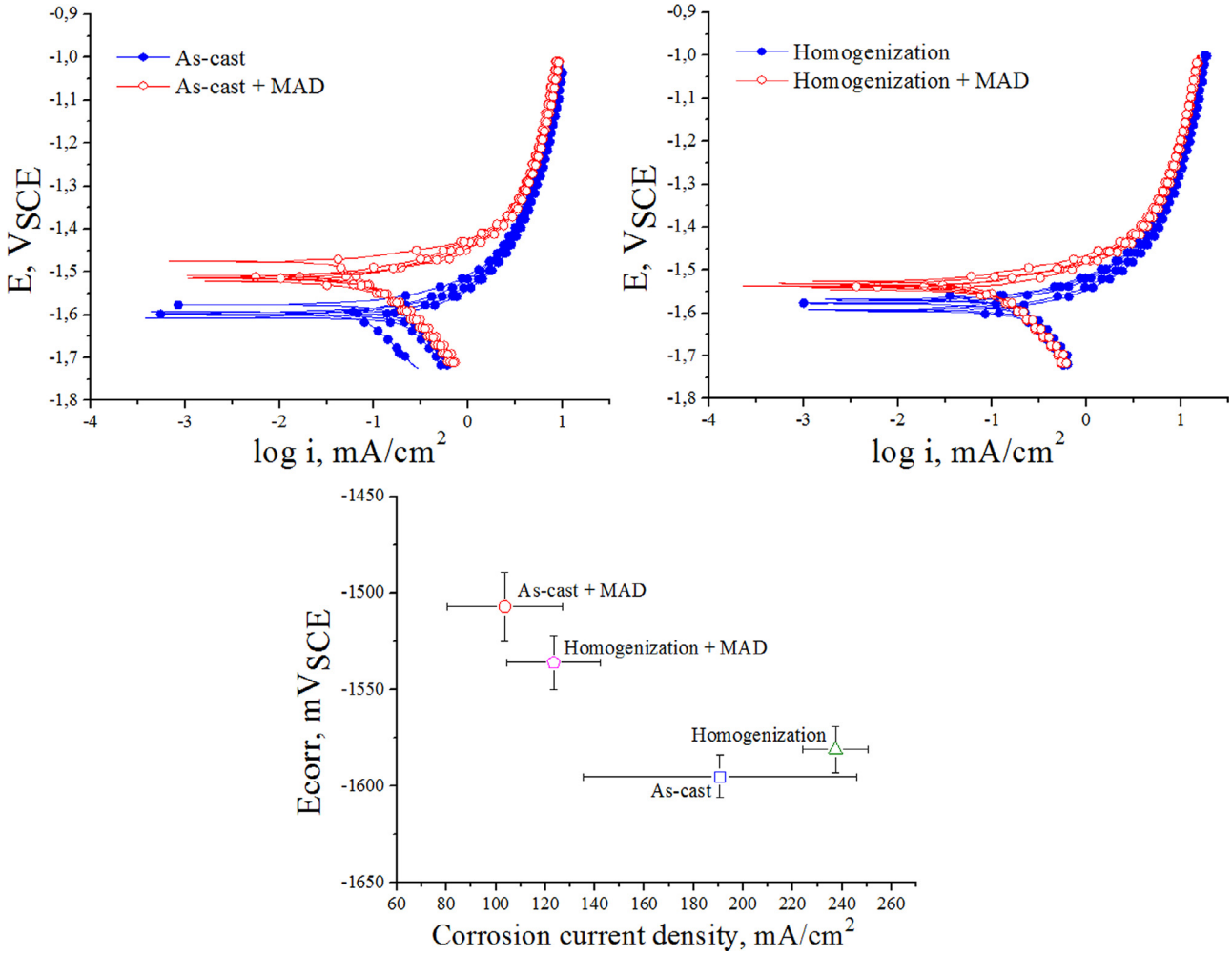

Fig. 13. Polarization curves (potential E in volt with respect to a saturated calomel electrode (SCE) vs. current density j) in 0.9% NaCl solution (pH = 7): (a) in the as-cast condition and after MAD and (b) in the annealed (homogenized) condition and after MAD. The values of the corrosion potential and the current density for the specimens with different processing histories are seen in (c).

observed within the recrystallized grains (Fig. 5c). By contrast, after the 9th pass, at the end temperature of 250 °C, a well-recrystallized microstructure with the HABs fraction of 69.3% was formed (Fig. 5e).

The presented results also permit evaluating the effect of the initial condition (as-cast *vs.* annealed) on the structure and properties of the alloy produced by MAD and/or uniaxial compression. Note that the primary goal of annealing in the present case was to dissolve Mg_2Ca second-phase particles. According to the equilibrium binary Mg-Ca phase diagram, as much as ~1.3 wt.% of Ca can be dissolved in a Mg-Ca solid solution at 510°C [45]. However, this goal was only partially achieved, as no full dissolution of particles was attained. The volume fraction of the particles decreased from 4.7% in the as-cast condition (Fig. 1a) to 2.5% after annealing at 510°C for 6 hours and quenching (Fig. 1b). Partial dissolution of Mg_2Ca in the as-cast and the annealed conditions was accompanied with an increase of Ca concentration in the Mg-based solid solution from 0.29 to 0.57 wt.%. A strong correlation between the observed changes in the volume fraction of the particles (a decrease by about one half) and nearly a doubling of the Ca concentration in the Mg matrix was observed. Most probably, an adjustment of the annealing conditions (in terms of temperature and time) is required to completely dissolve the particles. However, a further increase of the annealing temperature is problematic since the solidus temperature of the alloy is 516.5°C [45]. Further work on establishing optimal heat treatment conditions for the alloy is required, which is beyond the scope of the current study.

Although the alloy in the as-cast and the annealed conditions contained different amounts of Mg_2Ca particles prior to MAD, the variations in the particle fraction after 9 passes of MAD were insignificant: 7.1 and 7.3%, respectively (Fig. 8). However, the genesis of these particles was different. For the as-cast alloy, the fraction of particles increased only from 4.7 to 6.1% after MAD. This means that the majority of the particles were "inherited" from the initial as-cast condition, where the particles were mostly coarse and irregularly shaped (Fig. 7a). By contrast, for the annealed condition, the MAD resulted in gradual increase in the volume fraction of these particles from 2.7 to 6.5-7.3%, i.e. by a factor of 2.4-2.7 (Fig. 7). It can thus be surmised that most of the particles found in the annealed alloy after MAD processing have precipitated during deformation (and possibly also due to heating to the deformation temperature). These particles were much finer than the coarse particles that were found prior to deformation, although they exhibited pronounced growth during deformation (Fig. 6). As a result, the average particle size was much lower in the annealed + deformed alloy, *viz.* 1.0 μm against 1.6 μm in the as-cast + deformed condition.

The second-phase particles are known to have an effect on the microstructure development in Mg matrix during MAD [46]. DDRX involves migration of boundaries of new defect-free grains toward the interior of older deformed grains [43]. The particles can pin the moving boundaries via the well-known Zener drag mechanism [47]. Following Zener's original consideration, the pinning pressure P_Z on a boundary caused by homogeneously distributed spherical particles can be expressed as:

$$PZ = 3\gamma\frac{F_y}{d}, \quad (3)$$

where γ is the boundary surface energy per unit area, and F_y and d denote the volume fraction and the size of the dispersed particles, respectively.

As the particles in the annealed condition were finer and yet had similar volume fractions to those in the as-cast state at the most deformation temperatures (Fig. 7), the pinning pressure in the annealed state should have been greater. The higher pressure is likely to be the reason for the finer grain size of the annealed alloy after MAD in comparison with the as-cast condition (2.1 and 2.7 μm, respectively, see above). The presence of finer, more homogeneously distributed particles (Fig. 9) can also be the reason for more recrystallized structure with a greater fraction of HABs in the annealed alloy (Fig. 8). On the other hand, coarse (>1 μm) particles can potentially accelerate recrystallization due to the so-called particle-stimulated nucleation (PSN) [47], i.e. formation of specific deformation zones around particles that can serve as preferential nucleation sites for new grains. However, in the present case no evidence for PSN was found in our experiments (Figs. 3,5,8).

We should mention some inconsistencies between the microstructures observed in the Mg-0.8% Ca alloy after MAD finishing at 250°C and uniaxial compression at 250-350°C. While after MAD the effect of the initial condition (either as-cast or annealed) was insignificant (Fig. 9), distinctly different microstructures strongly influenced by the initial conditions were observed after uniaxial compression (Fig. 4a-d). This was not the case for compression at 450°C, which produced quite similar structures for the two initial states (Fig. 4e, f). Therefore, it can be conjectured that the differences in the initial structures were removed during initial stages of MAD. This is at variance with the microstructure evolution and mechanical behavior of the alloy during uniaxial compression at 250-350°C, which was affected by the initial microstructural state. Most probably, the effect is related to the difference in the concentration of Ca in α-Mg matrix and/or the volume fraction of the second-phase particles in the as-cast and the as-annealed material. Further studies are required to establish the exact reason for the mentioned differences, which, again, are beyond the scope of the present paper.

The present investigation of the mechanical properties of the Mg-0.8% Ca alloy showed that the ultimate tensile strength in the as-cast state was higher than that in the annealed one. After MAD, the UTS of the initially annealed samples was higher (Table 3). The fact that the ultimate tensile strength in the as-cast state is higher than in the annealed one can be explained by finer grains (61 μm *vs.* 95 μm) and a greater volume fraction of the particles (4.7% *vs.* 2.5%) in the former condition. The reversal of the tensile performance after MAD, i.e. the observation that the tensile strength of the as-annealed material was higher than that of the as-cast one can be associated with a smaller grain size (2.0 μm *vs.*

Table 4
Orientation factors for main slip systems and the $\{10\bar{1}2\} < 10\bar{1}1 >$ twinning systems of the Mg-0.8% Ca alloy.

State	Basal	Prismatic	Pyramidal	Twinning
As-cast	4.558	4.981	4.600	4.624
Annealed	4.507	4.790	4.796	4.885
As-cast + MAD	6.259	3.960	5.235	5.118
Annealed + MAD	4.595	4.651	5.494	5.980

2.7 μm) and a higher volume fraction of the particles (6.5% vs 6.1%) in the latter.

The ductility of magnesium alloys is generally strongly dependent on texture. The analysis of the orientation factors of the as-cast alloy after MAD has revealed a significant weakening of the activity of basal slip, pyramidal slip, and twinning in the $\{10\bar{1}2\} < 10\bar{1}1 >$ system with the concomitant activation of intense prismatic slip (Table 4). By contrast, MAD of the annealed alloy activates the basal slip and, to a degree, weakens the activity of prismatic slip. The corresponding orientation factors for these slip systems become close, and plastic deformation occurs mainly by basal and prismatic slip. Such changes in the orientation factors are most likely caused by the occurrence of preferred orientations of dynamically recrystallized grains. The emergence of these preferred orientations is associated with the precipitation of second-phase particles due to the decomposition of the supersaturated solid solution after MAD of the annealed alloy. A higher tensile elongation after MAD of the as-cast alloy compared to the annealed one was recorded. This can be explained by a lower concentration of particles in the former case. A further factor is the activation of the prismatic and pyramidal slip as well as twinning in the as-cast alloy. Their combined effect turns out to outperform the effect of the basal slip activation after MAD of the annealed alloy. In summary, it can be stated that the MAD processing of the Mg-0.8% Ca both in the as-cast state and in the annealed condition gives rise to a substantial increase of both strength and tensile ductility of the alloy.

There are conflicting reports on the effect of SPD on the corrosion characteristics of Mg alloys. On the one hand, an increase of the corrosion resistance of Mg and its alloys after ECAP or MAD treatment was reported in a number of publications [31,48-50]. On the other hand, a negative effect of SPD on the corrosion resistance was reported in [51,52]. Note that better corrosion characteristics were obtained in tests performed in environments with a low concentration of Cl^- ions, whereas an increase in the Cl^- concentration has led to the opposite behavior [51]. This might be an indication that the formation of a protective layer on the surface of the UFG magnesium alloys might be at play. Such a layer would likely provide protection only against non-aggressive environments with a low Cl- concentration [51].

The effect of grain size in UFG Mg-based alloys on their corrosion rate was investigated in several studies [52-54]. Generally, a finer grain structure leads to a lower corrosion rate in less aggressive environments. It was also found that chemical inhomogeneity, as well as the evolution of the volume fraction and spatial distribution of intermetallic particles during SPD can strongly affect the corrosion resistance [49].

In our case, an increase in the corrosion resistance and a decrease in the corrosion rate in an 0.9%NaCl solution after MAD of the alloy can be attributed to a significant grain refinement, an increase in the uniformity of the distribution of microstructure constituents, and the ensuing decrease of the proclivity for pitting nucleation. An increase of corrosion resistance may also be associated with a decrease in the surface roughness due to the grain refinement in the samples. The corrosion resistance of the MAD-modified material is further improved over that of the unprocessed one owing to a more evenly distributed fine Mg_2Ca particles. A factor contributing to the corrosion properties of SPD processed materials is a large number of crystal lattice defects accumulated in the course of deformation. Usually these defects are detrimental to the corrosion resistance. Discontinuous dynamic recrystallization is known to reduce the defect density [43], which may have a positive effect on the corrosion resistance of the alloy.

It should be noted again that the corrosion potential and the current density in both pre-MAD states of the alloy considered were the same within the error of measurement. This may stem from similar microstructures of the alloy in the as-cast and the as-annealed states. In both states, the microstructure comprises a magnesium-based solid solution and the Mg_2Ca phase, which is distributed relatively evenly both at the boundaries and in the grains. The structures differ only in the amount of the Mg_2Ca phase, which is slightly lower after homogenization by annealing. MAD leads to an increase in the corrosion potential and a reduction of the corrosion current density, which is tantamount to an increase of the corrosion resistance and a drop of the degradation rate. These characteristics of corrosion were found to be nearly the same, within the experimental error, for both initial states. This similarity of the corrosion characteristics can be explained by the similarity of the MAD-induced microstructures, as quantified by the respective grain sizes of 2.0 and 2.7 μm, Mg_2Ca particle sizes of 1.0 and 1.6 μm, and the Mg_2Ca volume fractions of 6.5 and 6.1%.

Table 5 shows the results of comparison of the mechanical properties and corrosion resistance of the Mg-0.8%Ca alloy obtained in the current work with the properties previously obtained using other treatments of the Mg-(0.8-1)%Ca alloys.

Thus, the corrosion potential of the as-cast Mg-0.8%Ca alloy noticeably exceeds the corrosion potential of the MAD-treated alloy and amounts to -1.73 ± 0.01 V, while the corrosion current density of the last one is higher [55]. At the same time, the corrosion resistance of the extruded Mg-0.79% Ca alloy is close to the values obtained after MAD (-1.59 V and 99.8 $\mu A/cm^2$ for the corrosion potential and the current density, respectively). However, it should be noted that the ultimate tensile strength of the extruded Mg-0.79%Ca alloy was appreciably lower than the strength of the MAD-treated Mg-0.8% Ca alloy (in both initial states) [58]. It is also noteworthy that the corrosion potential of the alloy obtained in the

Table 5
Comparison of mechanical properties and degradation rate of bioresorbable Mg–Ca alloys.

Alloy	YS, MPa	UTS, MPa	EL, %	Electrolyte solution	Corrosion potential, V	Current density, μA/cm^2	Reference
Mg-0.8% Ca, As-cast + MAD	199	264	9.4	0.9% NaCl solution	-1.507 ± 18 (SCE)	103.63 ± 23.30	Present study
Mg-0.8% Ca, Annealed + MAD	193	308	7.2		-1.536 ± 9 (SCE)	123.36 ± 19.03	
Mg-0.8% Ca, As-cast	-	-	-	Hanks' balanced salt solution	-1.73 ± 0.01 (SCE)	50 ± 10	[55]
Mg-1%Ca, ECAP	110	200	7	-	-	-	[56]
Mg-1%Ca, HPT	229.4±7.6	315.6±20.7	1.6±0.3	-	-	-	[57]
Mg-0.79%Ca, Extrusion	-	~195	-	Hanks' solution	~-1.59 (SCE)	99.8	[58]
Mg-1%Ca, As-cast	~40	71.38±3.01	1.87±0.14	SBF	~-1.89 (SCE)	-	[59]
Mg-1%Ca, Hot Rolling	~125	166.7±3.01	3±0.78		~-1.93 (SCE)	-	
Mg-1%Ca, Hot Extrusion	~130	239.63±7.21	10.63±0.64		~-1.75 (SCE)	-	
Mg-1%Ca, Extrusion	185.1±3.0	239.3±10.0	19.5±2.6	Hanks' solution	−1.65±0.02 (SCE)	8.45±1.61	[60]

present study is the lowest compared to the corrosion potential of the Mg-0.8% Ca and Mg-1% Ca alloys processed by extrusion and hot rolling, although the corrosion current density slightly exceeds the previously obtained values [58-60]. At the same time, the strength values obtained by the combined treatment (annealing + MAD) are close to the values obtained previously on the Mg-1% Ca alloy by high-pressure torsion. The greatest benefit of MAD processing was the enhanced tensile ductility of the Mg-0.8%Ca alloy. It outperformed the HPT-treated Mg-1% Ca alloy in terms of tensile elongation by far (7.2% and 1.6±0.3%, respectively) [57].

To sum up, the results of the current study showed that MAD can be effectively utilized to refine the microstructure of the Mg-0.8% Ca alloy, which is regarded to be promising for biomedical applications. The MAD-induced microstructural changes improve the mechanical characteristics (strength and ductility) of the alloy, as well as its corrosion resistance in NaCl solution. The resulting microstructures and properties of the alloy were found to be somewhat sensitive to its initial state (as-cast or as-annealed) prior to MAD. The observed effect was mostly attributed to dynamic precipitation of second-phase particles in the annealed alloy. The findings obtained provide valuable guidance for development of processing routes for this and other biomedical Mg alloys in a quest for attaining advanced mechanical and functional properties.

5. Conclusions

1. The multiaxial deformation (MAD) of the annealed Mg-0.8% Ca alloy with stepwise drops of temperature between the MAD passes was shown to produce a refined microstructure amenable to improved mechanical and corrosion performance of the alloy.
2. The principal mechanism responsible for the structure formation during MAD of the Mg-0.8% Ca alloy in the temperature range involved in the multi-pass processing (450-250 °C) was associated with dynamic recrystallisation – both continuous and discontinuous. This assertion is still hypothetical and calls for further investigation.
3. No texture was present in the as-cast alloy. Annealing resulted in the formation of a weak texture of the prismatic and deflected basal types with a total fraction of 0.14. MAD of the as-cast alloy led to the formation of a rather sharp prismatic texture with the fraction of the main orientations of 0.23. After MAD of the annealed alloy, the {00.4} basal poles moved from the periphery to the center of the pole figure and the sharpness of the maxima became weaker. The fraction of the non-texture component rose to 0.9.
4. The microstructure refinement by MAD was accompanied with a substantial improvement in the mechanical properties of the Mg-0.8% Ca alloy. Thus, the yield strength increased by a factor of ~4, to 193-199 MPa. The ultimate tensile strength after MAD of the annealed material reached 308 MPa, while that of the as-cast and subsequently deformed one was 264 MPa. The ductility, as determined by tensile elongation, also rose by a factor of ~ 2, to 7.2-9.4 %.
5. Within the measurement error, the corrosion potential and the corrosion current density of the as-cast and annealed samples of the Mg-0.8% Ca alloy, measured by the potentiodynamic polarization method, were nearly the same. MAD was found to improve the corrosion resistance considerably, along with a reduction of the corrosion rate.
6. As an overall takeaway conclusion, it can be asserted that MAD processing of Mg-0.8% Ca leads to a favorable combination of mechanical and corrosion properties, which qualifies the alloy as a candidate for applications in resorbable medical devices.

Acknowledgments

This work was supported by the Russian Science Foundation (Grant No. 18-45-06010) and within the framework of state task No. 075-00328-21-00 (texture study).

References

[1] L. Mordike, T. Ebert, Magnesium: properties-applications-potential, Mater Sci Eng A 302 (2001) 37–45, doi:10.1016/S0921-5093(00)01351-4.

[2] L.L. Rokhlin, Magnesium alloys containing rare earth metals: structure and properties, in: J.N. Fridlyander, D.G. Eskin (Eds.), Advances in metallic alloys, Taylor & Francis Ltd., London, UK, 2003.

[3] S. Virtanen, Biodegradable Mg and Mg alloys: Corrosion and biocompatibility, Mater Sci Eng B 176 (2011) 1600–1608, doi:10.1016/j.mseb.2011.05.028.

[4] S. Agarwal, J. Curtin, B. Duffy, et al., Biodegradable magnesium alloys for orthopaedic applications: a review on corrosion, biocompatibility and surface modifications, Mater Sci Eng C 68 (2016) 948–963, doi:10.1016/j.msec.2016.06.020.

[5] R. Waksman, Biodegradable stents: they do their job and disappear, J Invasive Cardiol 18 (2) (2006) 70–74.

[6] L. Tan, X. Yu, P. Wan, et al., Biodegradable materials for bone repairs: a review, J Mater Sci Technol 29 (6) (2013) 503–513, doi:10.1016/j.jmst.2013.03.002.

[7] Y.F. Zheng, X.N. Gu, F. Witte, Biodegradable metals, Mater Sci Eng R 77 (2014) 1–34, doi:10.1016/j.mser.2014.01.001.

[8] Y. Chen, Z. Xu, C. Smith, et al., Recent advances on the development of magnesium alloys for biodegradable implants: review, Acta Biomater 10 (2014) 4561–4573, doi:10.1016/j.actbio.2014.07.005.

[9] C. Castellani, R.A. Lindtner, P. Hausbrandt, et al., Bone-implant interface strength and osseointegration: Biodegradable magnesium alloy versus standard titanium control, Acta Biomater 7 (1) (2011) 432–440, doi:10.1016/j.actbio.2010.08.020.

[10] L. Mao, L. Shen, J. Niu, et al., Nanophasic biodegradation enhances the durability and biocompatibility of magnesium alloys for the next-generation vascular stents, Nanoscale 5 (20) (2013) 9517–9522, doi:10.1039/c3nr02912c.

[11] Y. Liu, S. Zheng, N. Li, et al., Study on the in vitro degradation behavior of pure Mg and WE43 in human bile for 60 days for future usage in biliary, Mater Lett 179 (2016) 100–103, doi:10.1016/j.matlet.2016.05.042.

[12] F. Feyerabend, J. Fischer, J. Holtz, et al., Evaluation of short-term effects of rare earth and other elements used in magnesium alloys on primary cells and cell lines, Acta Biomater 6 (5) (2010) 1834–1842, doi:10.1016/j.actbio.2009.09.024.

[13] R.Z. Valiev, A.P. Zhilyaev, T.G. Langdon, Bulk nanostructured materials: fundamentals and applications, Wiley, Hoboken, 2014.

[14] S.A. Alsubaie, P. Bazarnik, M. Lewandowska, et al., Evolution of microstructure and hardness in an AZ80 magnesium alloy processed by high-pressure torsion, J Mater Res Technol 5 (2) (2016) 152–158, doi:10.1016/j.jmrt.2015.11.006.

[15] J. Stráská, M. Janeček, J. Gubicza, et al., Evolution of microstructure and hardness in AZ31 alloy processed by high pressure torsion, J Alloys Compd 743 (2018) 437–447, doi:10.1016/j.msea.2014.12.005.

[16] A.S.J. Al-Zubaydi, A.P. Zhilyaev, S.C. Wang, et al., Superplastic behaviour of AZ91 magnesium alloy processed by high-pressure torsion, Mater Sci Eng A 637 (2015) 1–11, doi:10.1016/j.msea.2015.04.004.

[17] C. Chiu, S.-J. Huang, T.-Y. Chou, et al., Improving hydrogen storage performance of AZ31 Mg alloy by equal channel angular pressing and additives, J Alloys Compd 743 (2018) 437–447, doi:10.1016/j.jallcom.2018.01.412.

[18] M.A. Afifi, Y.C. Wang, P.H.R. Pereira, et al., Characterization of precipitates in an Al-Zn-Mg alloy processed by ECAP and subsequent annealing, Mater Sci Eng A 712 (2018) 146–156, doi:10.1016/j.msea.2017.11.091.

[19] L. Pantělejev, R. Štěpánek, O. Man, Thermal stability of bimodal microstructure in magnesium alloy AZ91 processed by ECAP, Mater Charact 107 (2015) 167–173, doi:10.1016/j.matchar.2015.07.009.

[20] N.S. Martynenko, E.A. Lukyanova, V.N. Serebryany, et al., Increasing strength and ductility of magnesium alloy WE43 by equal-channel angular pressing, Mater Sci Eng A 712 (2018) 625–629, doi:10.1016/j.msea.2017.12.026.

[21] R.Z. Valiev, Y. Estrin, Z. Horita, et al., Producing bulk ultrafine-grained materials by severe plastic deformation, JOM 58 (2006) 33–39, doi:10.1007/s11837-006-0213-7.

[22] S.V. Dobatkin, L.L. Rokhlin, G.A. Salishchev, et al., Structure and properties of an Mg–0.3% Ca magnesium alloy after multiaxial deformation and equal channel angular pressing, Russ Met 2014 (11) (2014) 911–919, doi:10.1134/S003602951411007X.

[23] D.R. Nugmanov, O.S. Sitdikov, M.V. Markushev, Structure of magnesium alloy MA14 after multistep isothermal forging and subsequent isothermal rolling, Phys Met Metall 116 (10) (2015) 993–1001, doi:10.1134/S0031918x15080116.

[24] A. Salandari-Rabori, A. Zarei-Hanzaki, S.M. Fatemi, et al., Microstructure and superior mechanical properties of a multi-axially forged WE magnesium alloy, J Alloys Compd 693 (2017) 406–413, doi:10.1016/j.jallcom.2016.09.198.

[25] A. Salandari-Rabori, A. Zarei-Hanzaki, H.R. Abedi, et al., Micro and macro texture evolution during multiaxial forging of a WE43 magnesium alloy, J Alloys Compd 739 (2018) 249–259, doi:10.1016/j.jallcom.2017.12.181.

[26] G.E. Poinern, S. Brundavanam, D. Fawcett, Biomedical magnesium alloys: a review of material properties, surface modifications and potential as a biodegradable orthopaedic implant, Am J Biomed Eng 296 (2012) 218–240, doi:10.5923/j.ajbe.20120206.02.

[27] J. Li, J. Wongsa-Ngam, J. Xu, et al., Wear resistance of an ultrafine-grained Cu-Zr alloy processed by equal-channel angular pressing, Wear 326-327 (2015) 10–19, doi:10.1016/j.wear.2014.12.022.

[28] M.I. Abd El Aal, N. El Mahallawy, F.A. Shehata, et al., Wear properties of ECAP-processed ultrafine grained Al–Cu alloys, Mater Sci Eng A 527 (2010) 3726–3732, doi:10.1016/j.msea.2010.03.057.

[29] G. Purcek, H. Yanar, D.V. Shangina, et al., Improvement of mechanical and tribological properties of Cu–Cr–Zr alloy by high pressure torsion and aging, J Alloys Compd 742 (2018) 325–333, doi:10.1016/j.jallcom.2018.01.303.

[30] B. Hadzima, M. Janecek, Y. Estrin, et al., Microstructure and corrosion properties of ultrafine-grained interstitial free steel, Mater Sci Eng A 462 (2007) 243–247, doi:10.1016/j.msea.2005.11.081.

[31] S.V. Dobatkin, E.A. Lukyanova, N.S. Martynenko, et al., Strength, corrosion resistance, and biocompatibility of ultrafine-grained Mg alloys after different modes of severe plastic deformation, IOP Conf Ser Mater Sci Eng 194 (2017) 012004, doi:10.1088/1757-899X/194/1/012004.

[32] S. Dobatkin, J. Zrnik, I. Mamuzic, Ultrafine-grained low carbon steels by severe plastic deformation, Metalurgija 47 (3) (2008) 181–186.

[33] Y. Furuya, S. Matsuoka, S. Shimakura, et al., Effect of carbon and phosphorus addition on the fatigue roperties of ultrafine-grained steels, Scripta Mater 52 (2005) 1163–1167, doi:10.1016/j.scriptamat.2005.01.035.

[34] M. Okayasu, K. Sato, M. Mizuno, et al., Fatigue properties of ultra-fine grained dual phase ferrite/martensite low carbon steel, Int J Fatigue 30 (2008) 1358–1365, doi:10.1016/j.ijfatigue.2007.10.011.

[35] S.V. Dobatkin, W. Skrotzki, O.V. Rybalchenko, et al., Structural changes in metastable austenitic steel during equal channel angular pressing and subsequent cyclic deformation, Mater Sci Eng A 723 (2018) 141–147, doi:10.1016/j.msea.2018.03.018.

[36] A. Vinogradov, V. Patlan, Y. Suzuki, et al., Structure and properties of ultra-fine grain Cu–Cr–Zr alloy produced by equal-channel angular pressing, Acta Mater 50 (2002) 1639–1651, doi:10.1016/S1359-6454(01)00437-2.

[37] D.V. Shangina, N.R. Bochvar, M.V. Gorshenkov, et al., Influence of microalloying with zirconium on the structure and properties of Cu–Cr alloy after high pressure torsion, Mater Sci Eng A 650 (2016) 63–66, doi:10.1016/j.msea.2015.10.008.

[38] T.I. Savyolova, S.F. Kourtasov, ODF restoration by orientation grid, Mater Sci Forum 495–497 (2005) 301–306, doi:10.4028/www.scientific.net/MSF.495-497.301.

[39] V.N. Serebryany, T.M. Ivanova, T.I. Savyolova, et al., Effect of texture on tensile properties of an ECAP-processed MA2-1 magnesium alloy, Solid State Phenomena 160 (2010) 159–164, doi:10.4028/www.scientific.net/SSP.160.159.

[40] N.T. Kirkland, N. Birbilis, M.P. Staiger, Assessing the corrosion of biodegradable magnesium implants: A critical review of current methodologies and their limitations, Acta Biomater 8 (2012) 925–936, doi:10.1016/j.actbio.2011.11.014.

[41] N.T. Kirkland, N. Birbilis, J. Walker, et al., In-vitro dissolution of magnesium–calcium binary alloys: clarifying the unique role of calcium additions in bioresorbable magnesium implant alloys, J Biomed Mater Res B 95B (2010) 91–100, doi:10.1002/jbm.b.31687.

[42] Z. Li, X. Gu, S. Lou, et al., The development of binary Mg-Ca alloys for use as biodegradable materials within bone, Biomaterials 29 (2008) 1329–1344, doi:10.1016/j.biomaterials.2007.12.021.

[43] F.J. Humphreys, M. Hatherly, Recrystallization and related annealing phenomena, 1st Edition, Pergamon, Netherlands, 1996.

[44] A. Galiev, R. Kaibyshev, G. Gottstein, Correlation of plastic deformation and dynamic recrystallization in magnesium alloy ZK60, Acta Mater 49 (2001) 1199–1207, doi:10.1016/S1359-6454(01)00020-9.

[45] B. Predel. Ca - Mg (Calcium - Magnesium). In: Predel B. (eds) B - Ba … Cu - Zr. Landolt-Börnstein - Group IV Physical Chemistry (Numerical Data and Functional Relationships in Science and Technology), vol 12B. Springer, Berlin, Heidelberg, 2012. (https://doi.org/10.1007/978-3-540-44756-6_114).

[46] K. Huang, K. Marthinsen, Q. Zhao, et al., The double-edge effect of particles on the recrystallization behaviour and associated mechanical properties of metallic materials, Prog Mater Sci 92 (2018) 284–359, doi:10.1016/j.pmatsci.2017.10.004.

[47] C.S. Smith, Introduction to grains, phases, and interfaces: an interpretation of microstructure, Trans Am Inst Min Eng 175 (1948) 15–51 https://www.sciencedirect.com/science/article/pii/S0079642517301287.

[48] C. Op"t Hoog, N. Birbilis, Y. Estrin, Corrosion of Pure Mg as a Function of Grain Size and Processing Route, Adv Eng Mater 10 (6) (2008) 579–582, doi:10.1002/adem.200800046.

[49] N. Birbilis, K.D. Ralston, S. Virtanen, et al., Grain character influences on corrosion of ECAPed pure magnesium, Corros Eng Sci Technol 45 (2010) 224–230 https://doi.org/10.1179/147842209 × 12559428167805.

[50] D. Orlov, K.D. Ralston, N. Birbilis, et al., Enhanced corrosion resistance of Mg alloy ZK60 after processing by integrated extrusion and equal channel angular pressing, Acta Mater 59 (2011) 6176–6186, doi:10.1016/j.actamat.2011.06.033.

[51] D. Song, A. Ma, J. Jiang, et al., Corrosion behavior of equal-channel-angular-pressed pure magnesium in NaCl aqueous solution, Corros Sci 52 (2) (2010) 481–490, doi:10.1016/j.corsci.2009.10.004.

[52] G.Ben Hamu, D. Eliezer, L. Wagner, The relation between severe plastic deformation microstructure and corrosion behavior of AZ31 magnesium alloy, J Alloy Compd 468 (1-2) (2009) 222–229, doi:10.1016/j.jallcom.2008.01.084.

[53] C. Op't Hoog, N. Birbilis, Y. Estrin, Corrosion of pure Mg as a function of grain size and processing route, Adv Eng Mater 10 (2008) 579–582, doi:10.1002/adem.200800046.

[54] K.D. Ralston, N. Birbilis, Effect of grain size on corrosion: a review, Corrosion 66 (7) (2010) 075005–075005-1, doi:10.5006/1.3462912.

[55] A. Mohamed, A.M. El-Aziz, H.-G. Breitinger, Study of the degradation behavior and the biocompatibility of Mg–0.8Ca alloy for orthopedic implant application, J Magnes Alloy 7 (2) (2019) 249–257, doi:10.1016/j.jma.2019.02.007.

[56] W. Li, Y. Shen, J. Shen, D. Shen, X. Liu, Y. Zheng, K.W.K. Yeung, S. Guan, O.B. Kulyasova, R.Z. Valiev, In vitro and in vivo studies on pure Mg, Mg–1Ca and Mg–2Sr alloys processed by equal channel angular pressing, Nano Mater Sci 2 (1) (2020) 96–108, doi:10.1016/j.nanoms.2020.03.004.

[57] X.Liu W/Li, Y. Zheng, W. Wang, W. Qiao, K.W.K. Yeung, K.M.C. Cheung, S. Guan, O.B. Kulyasova, R.Z. Valiev, In vitro and in vivo studies on ultrafine-grained biodegradable pure Mg, Mg-Ca alloy and Mg-Sr alloy processed by high-pressure torsion, Biomater Sci 8 (18) (2020) 5071–5087, doi:10.1039/d0bm00805b.

[58] W.-C.Qi R.-C.Zeng, H.-Z. Cui, F. Zhang, S.-Q. Li, E.-H. Han, In vitro corrosion of as-extruded Mg–Ca alloys — The influence of Ca concentration, Corros Sci 96 (2015) 23–31, doi:10.1016/j.corsci.2015.03.018.

[59] Z. Li, X. Gu, S. Lou, Y. Zheng, The development of binary Mg–Ca alloys for use as biodegradable materials within bone, Biomaterials 29 (10) (2008) 1329–1344, doi:10.1016/j.biomaterials.2007.12.021.

[60] Y.S. Jeong, W.J. Kim, Enhancement of mechanical properties and corrosion resistance of Mg–Ca alloys through microstructural refinement by indirect extrusion, Corros Sci 82 (2014) 392–403, doi:10.1016/j.corsci.2014.01.041.